



# Open Research Online

---

The Open University's repository of research publications and other research outputs

## Diurnal Variation in Martian Dust Devil Activity

### Journal Item

How to cite:

Chapman, R. M.; Lewis, S. R.; Balme, M. and Steele, L. J. (2017). Diurnal Variation in Martian Dust Devil Activity. *Icarus*, 292 pp. 154–167.

For guidance on citations see [FAQs](#).

© 2017 The Authors

Version: Accepted Manuscript

Link(s) to article on publisher's website:

<http://dx.doi.org/doi:10.1016/j.icarus.2017.01.003>

---

Copyright and Moral Rights for the articles on this site are retained by the individual authors and/or other copyright owners. For more information on Open Research Online's data [policy](#) on reuse of materials please consult the policies page.

---

[oro.open.ac.uk](http://oro.open.ac.uk)

# Accepted Manuscript

Diurnal Variation in Martian Dust Devil Activity

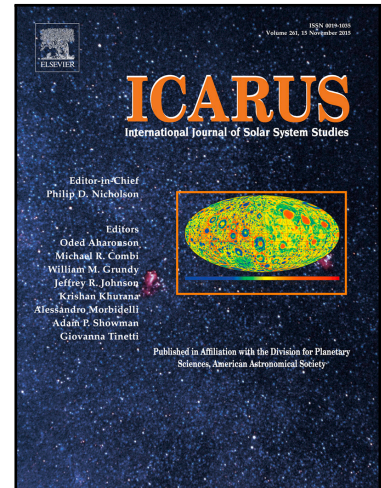
R.M. Chapman, S.R. Lewis, M. Balme, L.J. Steele

PII: S0019-1035(16)30289-5  
DOI: [10.1016/j.icarus.2017.01.003](https://doi.org/10.1016/j.icarus.2017.01.003)  
Reference: YICAR 12325

To appear in: *Icarus*

Received date: 15 June 2016  
Revised date: 4 January 2017  
Accepted date: 4 January 2017

Please cite this article as: R.M. Chapman, S.R. Lewis, M. Balme, L.J. Steele, Diurnal Variation in Martian Dust Devil Activity, *Icarus* (2017), doi: [10.1016/j.icarus.2017.01.003](https://doi.org/10.1016/j.icarus.2017.01.003)



This is a PDF file of an unedited manuscript that has been accepted for publication. As a service to our customers we are providing this early version of the manuscript. The manuscript will undergo copyediting, typesetting, and review of the resulting proof before it is published in its final form. Please note that during the production process errors may be discovered which could affect the content, and all legal disclaimers that apply to the journal pertain.

**Highlights**

- Modelled Martian dust devil activity occurs earlier in the sol than expected.
- Peak dust devil activity occurs during morning hours across multiple areas.
- Dust devil diurnal variability is governed by local wind speeds.
- Model results show good match to surface observations of dust devil timings.
- Dust devil parameterisation in Mars Global Circulation Models is incomplete.

ACCEPTED MANUSCRIPT

# Diurnal Variation in Martian Dust Devil Activity

R. M. Chapman<sup>a,\*</sup>, S. R. Lewis<sup>a</sup>, M. Balme<sup>a</sup>, L. J. Steele<sup>a</sup>

<sup>a</sup>*The Open University, Walton Hall, Milton Keynes, MK7 6AA, UK*

---

## Abstract

We show that the dust devil parameterisation in use in most Mars Global Circulation Models (MGCMs) results in an unexpectedly high level of dust devil activity during morning hours.

Prior expectations of the diurnal variation of Martian dust devils are based mainly upon the observed behaviour of terrestrial dust devils: i.e. that the majority occur during the afternoon. We instead find that large areas of the Martian surface experience dust devil activity during the morning in our MGCM, and that many locations experience a peak in dust devil activity before mid-sol.

We find that the diurnal variation in dust devil activity is governed by near-surface wind speeds. Within the range of daylight hours, higher wind speeds tend to produce higher levels of dust devil activity, rather than the activity simply being governed by the availability of heat at the planet's surface, which peaks in early afternoon.

Evidence for whether the phenomenon we observe is real or an artefact of the parameterisation is inconclusive. We compare our results with surface-based observations of Martian dust devil timings and obtain a good match with the majority of surveys. We do not find a good match with orbital observations, which identify a diurnal distribution more closely matching that of terrestrial dust devils, but orbital observations have limited temporal coverage, biased towards the early afternoon.

We propose that the generally accepted description of dust devil behaviour on Mars is incomplete, and that theories of dust devil formation may need to be modified specifically for the Martian environment. Further surveys of dust devil observations are required to support any such modifications. These surveys should include both surface and orbital observations, and the range of observations must encompass the full diurnal period and consider the wider meteorological context surrounding the observations.

*Keywords:* Mars, atmosphere, Mars, climate, Mars, surface

---

## 1. Introduction

Dust is present within the atmosphere of Mars as a constant background haze (Pollack et al., 1977; Martin, 1986; Smith et al., 2001). Martian dust devils were first identified in Viking Orbiter images (Thomas and Gierasch, 1985) and have since been observed

---

\*Corresponding author

*Email address:* [rhian.chapman@open.ac.uk](mailto:rhian.chapman@open.ac.uk) (R. M. Chapman)

*Preprint submitted to Elsevier*

*January 5, 2017*

5 in a large number of images captured by Mars orbiting spacecraft (Fisher et al., 2005;  
6 Stanzel et al., 2006), as well as in multiple images returned from rovers on the surface  
7 (Ferri et al., 2003; Greeley et al., 2006). The tracks left behind by the passage of dust  
8 devils – usually visible as dark streaks against the higher albedo surface – have also been  
9 observed in many orbiter images (Cantor et al., 2006).

10 Martian dust devils are named after the apparently similar features observed on Earth.  
11 These are near-surface atmospheric vortices that are visible due to the particles they lift  
12 from the ground and entrain in a vertical, upwardly-spiraling column of air. The core  
13 of a dust devil is commonly at a lower pressure than the surrounding vortex (Sinclair,  
14 1964). Dust devils are able to lift surface dust particles due to the wind shear stress  
15 present within the walls of the vortex (Balme et al., 2003a). The lower central pressure  
16 within the column may also contribute to dust lifting by providing an upwards force that  
17 assists the shear stress in overcoming interparticle cohesion forces (Greeley et al., 2003;  
18 Balme and Hagermann, 2006). Dust devil activity on Mars is highly variable between  
19 regions and seasons (Fisher et al., 2005), and Martian dust devils are more frequently  
20 observed in local spring and summer months (Thomas and Gierasch, 1985; Balme et al.,  
21 2003b; Cantor et al., 2006).

22 This work uses a Martian Global Circulation Model (MGCM) to investigate the  
23 diurnal variation in Martian dust devil activity. The rate of surface dust lifting by dust  
24 devils (henceforth termed “dust devil lifting”) was used as a proxy for assessing the level  
25 of dust devil activity at any specific location and time. No statements can be made about  
26 the number or size of dust devils represented by a specific level of activity.

27 In Section 2 we discuss the model parameterisation that simulates dust devils in the  
28 Martian atmosphere; in Section 3 we present the results from the model; in Section 4  
29 we explore in detail the components of the dust devil parameterisation and consider how  
30 our results compare against orbital and surface observations. Section 5 summarises this  
31 work and in Section 6 we detail our conclusions.

## 32 2. Method

33 The MGCM used in this work (henceforth referred to as “the MGCM”) is a global,  
34 multi-level spectral model of the Martian atmosphere up to an altitude of  $\sim 100$  km,  
35 as described by Forget et al. (1999). Simulations were completed at a resolution of  $5^\circ$   
36 latitude  $\times$   $5^\circ$  longitude, resulting in a gridbox at the equator measuring  $\sim 300 \times 300$  km.

37 Each simulation begins with a two-year ‘spin-up’ period from a dynamically static  
38 atmosphere, in order to allow the annual progression of tracer distributions to settle into  
39 representative cycles. The results analysed below correspond to the third full Mars Year  
40 (MY) of each simulation, starting at solar longitude  $L_S = 0^\circ$ . The prescribed atmo-  
41 spheric dust loadings used within these simulations correspond to daily global dust maps  
42 described by Montabone et al. (2015), which were obtained by binning and interpolation  
43 of spacecraft data. The Martian calendar adopted herein follows the approach proposed  
44 within Clancy et al. (2000). Following Lewis et al. (1999), a Martian ‘hour’ is 1/24th of  
45 a sol (a sol being a Martian day). All times herein that refer to surface-level phenomena  
46 relate to local times.

47 The dust devil parameterisation was implemented by Newman et al. (2002). The  
48 subroutine was modified by Mulholland (2012) to add a two-moment tracer scheme, but

49 the core of the parameterisation remained the same. Here, we outline the components  
 50 of this dust devil parameterisation; in Section 4, we assess in detail the impact of each  
 51 component on the diurnal timing of dust devil lifting.

52 The flux of surface dust lifted by dust devils within an MGCM gridbox,  $F_{\text{devil}}$ , is  
 53 calculated from the sensible heat flux,  $F_s$ , and the dust devil thermodynamic efficiency,  
 54  $\eta$ :

$$F_{\text{devil}} = \alpha_D \eta F_s \quad (1)$$

55 where  $\alpha_D$  is a tuneable parameter representing the ‘dust devil lifting efficiency’, required  
 56 due to the uncertainty surrounding the actual quantity of dust that Martian dust devils  
 57 are able to lift. The value of this parameter is set such that the total annual dust cycle  
 58 within a simulation best matches the range of observed dust opacities (Newman et al.,  
 59 2002). For the current resolution,  $\alpha_D = 1.13333 \times 10^{-8} \text{ kg J}^{-1}$ . This value is constant  
 60 throughout the simulation.

61 The quantity  $\eta$  arises from the modelling of a dust devil as a ‘heat engine’, following  
 62 Rennó et al. (1998).  $\eta$  is the thermodynamic efficiency of a dust devil: the fraction of  
 63 the input heat that is converted into mechanical work. This thermodynamic efficiency is  
 64 approximated as  $\eta \approx 1 - b$ , where

$$b = \frac{(p_{\text{surf}}^{\chi+1} - p_{\text{top}}^{\chi+1})}{(p_{\text{surf}} - p_{\text{top}})(\chi + 1)p_{\text{surf}}^{\chi}} \quad (2)$$

65 in which  $p_{\text{surf}}$  is the local surface pressure,  $p_{\text{top}}$  is the pressure at the top of the convective  
 66 boundary layer (CBL) within the Martian atmosphere, and  $\chi$  is equal to the specific gas  
 67 constant ( $R$ ) divided by the specific heat capacity at constant pressure ( $c_p$ ).

68 The sensible heat flux,  $F_s$ , represents the input heat available to drive the dust devil  
 69 ‘heat engine’, and can be written as:

$$F_s = \rho c_p C_D U (t_{\text{surf}} - t_{\text{atm}}) \quad (3)$$

70 where  $\rho$  is the near-surface atmospheric density,  $C_D$  is the surface drag coefficient,  $U$  is  
 71 the horizontal wind speed,  $t_{\text{surf}}$  is the surface temperature, and  $t_{\text{atm}}$  is the temperature  
 72 in the lowest layer of the atmosphere.

73 The surface drag coefficient  $C_D$  is parameterised using the classical expression for a  
 74 boundary layer drag coefficient (Esau, 2004):

$$C_D = \left( \frac{\kappa}{\ln(1 + z/z_0)} \right)^2 \quad (4)$$

75 where the von Kármán constant  $\kappa \approx 0.4$ ,  $z$  is the height of the lowest layer of the  
 76 atmosphere, and  $z_0$  is the surface roughness length. In these simulations  $z \sim 5$  m. The  
 77 surface roughness length was kept constant at  $z_0 = 0.01$  m, resulting in a constant value  
 78 of  $C_D$  across the planet’s surface.

79 The wind speed  $U$  is the magnitude of the near-surface wind speed, calculated from  
 80 the large-scale zonal and meridional wind components ( $u$  and  $v$ ) within the lowest layer  
 81 of the atmosphere.

82 The dust devil parameterisation in operation within the MGCM has been used as the  
 83 basis for similar parameterisations in other Mars atmospheric models. The NASA Ames

84 Mars General Circulation Model (GCM) directly incorporates the Newman et al. (2002)  
 85 parameterisation (Kahre et al., 2006, 2008), as does the Geophysical Fluid Dynamics  
 86 Laboratory (GFDL) Mars GCM parameterisation (Basu et al., 2004).

87 Surface dust was also lifted into the atmosphere through lifting by near-surface wind  
 88 stress, implemented within the MGCM following Newman et al. (2002) as modified by  
 89 Mulholland et al. (2013). Lifting by near-surface wind stress is thought to be the primary  
 90 dust lifting process associated with Martian dust storms (e.g. Strausberg et al. (2005),  
 91 Basu et al. (2006) and Wilson (2011)).

92 To provide comparison and validation datasets for the model results we have chosen to  
 93 use observations of Martian dust devils obtained from orbit and from the surface. Global  
 94 plots and histograms from the model output can be compared with orbital observations;  
 95 localised plots of model results can be compared with surface observations.

96 The gridboxes chosen for the localised analysis correlate as closely as possible with the  
 97 locations of Mars landers identified in Table 1. The daily cycle of dust devil lifting was  
 98 plotted for each location, taking into account the time of year and the local atmospheric  
 99 dust environment of the observations.

100 The simulations were completed using prescribed dust fields. In the current approach,  
 101 dust lifted by both dust devils and near-surface wind stress is combined into a total  
 102 atmospheric dust field, which is then scaled (at gridbox resolution) to match daily global  
 103 maps of the optical depth of the Martian atmosphere (Montabone et al., 2015). Dust from  
 104 both surface-level processes is treated as equivalent once it is within the atmosphere. The  
 105 local atmospheric dust environment during a lander’s observations can be approximated  
 106 using these fields: the modelled optical depth that would be reported at a surface location  
 107 in the vicinity of a lander’s position can be compared to the optical depth recorded by  
 108 that lander during its observations.

109 If a dust map has been constructed for the year in which a mission took place (for  
 110 example, the Phoenix mission landed in MY29), a simulation using the relevant atmo-  
 111 spheric dust loading was used for the comparison analysis. For missions that took place  
 112 before the earliest dust map observation (MY24, beginning in July 1998), the local op-  
 113 tical depth observed by the lander was compared with the local optical depth produced  
 114 by the MGCM simulations across multiple Mars years of differing atmospheric dust con-  
 115 ditions, and results from the closest match were then used for the analysis. Dust maps  
 116 are available from MY24 to MY32.

117 The amount of dust present in the atmosphere has an effect on dust devil lifting  
 118 primarily through its impact on surface and near-surface temperatures. Atmospheric  
 119 dust absorbs incident solar radiation, resulting in a heating of the atmosphere and a  
 120 reduction of surface insolation (Zurek, 1978). A high level of atmospheric dust, such  
 121 as that observed during dust storms, will therefore cause an increase in near-surface  
 122 atmospheric temperatures and a decrease in insolation-driven surface temperatures. This  
 123 reduces the surface-to-atmosphere temperature gradient ( $(t_{\text{surf}} - t_{\text{atm}})$  in Equation 3),  
 124 which lowers the amount of surface-level heat available to drive dust devil formation.

### 125 3. Results

126 From our simulation results we created global maps of the diurnal variation in dust  
 127 devil lifting. For each gridbox, dust devil lifting was calculated at 12 local times, spaced

Lander	Lander location (latitude/°N, longitude/°E)
Viking Lander 2 (VL2)	47.97, 134.25
Pathfinder	19.33, 33.55
Phoenix	68.22, 125.70
MER Spirit	-14.61, 175.47
MSL Curiosity	-4.59, 137.44

Table 1: Locations of NASA landers, Mars Exploration Rover (MER) Spirit and Mars Science Laboratory (MSL) Curiosity.

128 evenly through a sol. Dust devil lifting is somewhat stochastic in nature, varying from  
 129 sol to sol in both amplitude and timing, so to investigate trends, simulation results were  
 130 averaged over  $30^\circ$   $L_S$ -long sections of the Martian year. This allows the identification of  
 131 the time-of-sol at which dust devils are most commonly active within a given gridbox  
 132 during the analysed portion of the year: the ‘peak dust devil lifting’ time. (To eliminate  
 133 extremely low levels of dust devil lifting from subsequent calculations, a threshold dust  
 134 lifting rate was applied at this stage of the analysis. This threshold was set at  $1 \times 10^{-11}$   
 135  $\text{kg m}^{-2} \text{s}^{-1}$ , a value chosen by considering the dust lifting rates at the lander sites, see  
 136 Figures 4 and 5.)

137 An example of these global maps is shown in Figure 1, which displays the range of  
 138 timings in the daily peak dust devil lifting across the planet’s surface. This figure displays  
 139 data from the start of the Martian year ( $L_S = 0-30^\circ$ ), corresponding to early Northern  
 140 Hemisphere spring. Figure 2a shows the same data plotted as a histogram. These figures  
 141 identify a clear bimodal distribution of the diurnal timing of peak dust devil lifting, with  
 142 one peak evident in the mid-morning and one peak evident in the late afternoon.

143 The global diurnal variation of dust devil lifting changes through the year, displaying  
 144 a seasonal shift from a bimodal to unimodal distribution. Figure 2b displays a histogram  
 145 of data from the same simulation, but at a point in the year approaching perihelion,  
 146 corresponding to late Northern Hemisphere autumn ( $L_S = 210-240^\circ$ ). This figure displays  
 147 a unimodal timing distribution of peak dust devil lifting, with a single peak in the mid-  
 148 afternoon. Figure 3 shows histograms of all 12 such  $30^\circ$   $L_S$ -long sections of the Martian  
 149 year, illustrating the seasonal shift in the distribution.

150 Surface observations provide more dust devil lifting diurnal variation information  
 151 than orbital observations. We completed simulations for direct comparison with pre-  
 152 vious studies that use data from the four surface missions identified in Table 1. The  
 153 comparisons presented here for each landing site correspond to the times of year anal-  
 154 ysed by the previous studies. For the shorter duration missions, Pathfinder and Phoenix,  
 155 those studies covered the full length of the mission; for VL2 and Spirit, those studies  
 156 covered only a portion of the whole mission.

157 It should be noted that the majority of lander data reported within the comparison  
 158 studies are pressure detections of atmospheric vortices, with one study reporting directly  
 159 imaged dust devils (detailed in Section 4.2). The two data types are not completely  
 160 equivalent: although all dust devils are vortices, not all vortices entrain dust.

161 The following figures display the diurnal variation in dust devil lifting for each site.  
 162 The envelope encompassing all of the results obtained through the analysed time period



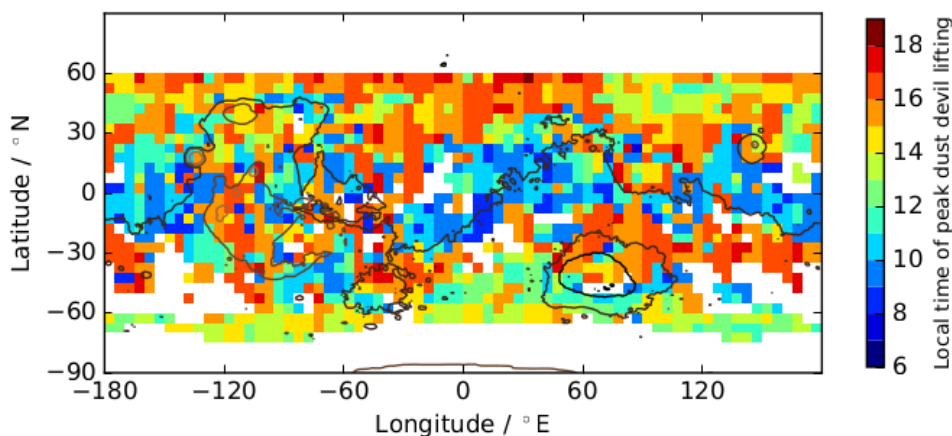


Figure 1: Global plot in which colour scale denotes the diurnal timing of peak dust devil lifting across the Martian surface. The data displayed here represent dust devil lifting averaged across  $L_S = 0-30^\circ$ , from a simulation using a relatively low atmospheric dust loading. Gridboxes coloured yellow, orange or red relate to afternoon peaks in dust devil lifting; blue gridboxes relate to morning peaks in dust devil lifting. White gridboxes indicate no lifting or below threshold lifting. Contour lines denoting topography are included for illustration only.

163 is shown, as well as the average across that period. Note that the amounts of dust lifted  
 164 vary by two orders of magnitude between the different lander sites.

165 The Viking Landers reached Mars during MY12, a year that experienced large dust  
 166 storms and subsequent high atmospheric dust loading. The visible optical depth observed  
 167 at the VL2 landing site during the earliest portion of the mission ( $L_S = 117-148^\circ$ ) was  
 168 reported as  $\sim 0.3-0.4$  (Pollack et al., 1977; Colburn et al., 1989). This is best matched  
 169 by the visible optical depth simulated in this region at this time of year in the MGCM  
 170 simulation using the MY25 dust field (MY25 also experienced a large dust storm later  
 171 in the year). Figure 4a shows analysed dust devil lifting in the vicinity of the VL2  
 172 landing site, alongside data from the comparison study by Ringrose et al. (2003). The  
 173 Pathfinder mission took place during MY23,  $L_S = 140-190^\circ$ . The visible optical depth  
 174 observed by the lander varied from  $\sim 0.4$  shortly after landing to  $\sim 0.6$  towards the end of  
 175 the mission (Smith and Lemmon, 1999). The MGCM simulation using the MY28 dust  
 176 field produces a visible optical depth of  $\sim 0.5$  in this region throughout the length of the  
 177 mission. Figure 4b shows analysed dust devil lifting in the vicinity of the Pathfinder  
 178 landing site, alongside data from the comparison study by Murphy and Nelli (2002).  
 179 The Phoenix mission landed in MY29, operating through  $L_S = 77-148^\circ$ . Figure 4c shows  
 180 analysed dust devil lifting in the vicinity of the Pathfinder landing site, alongside data  
 181 from the comparison study by Ellehoj et al. (2010). The long duration of the MER Spirit  
 182 mission enabled extended observations of dust devils, encompassing multiple years. The  
 183 annual dust devil ‘season’ observed by the rover spanned the second half of the year,  
 184  $L_S \sim 175-355^\circ$ . Three full dust devil seasons were observed by Spirit in the relevant  
 185 comparison study, spanning MY27-MY29. Figure 5 shows analysed dust devil lifting in  
 186 the vicinity of the Spirit operational site, alongside data from the comparison study by  
 187 Greeley et al. (2010). MSL Curiosity landed in MY31, beginning its ongoing mission on

188  $L_S = 150^\circ$ . Figure 4d shows analysed dust devil lifting in the vicinity of the Curiosity  
 189 site through the first full year (668 sols) of the rover's operation, alongside data from the  
 190 comparison study by Kahanpää et al. (2016).

#### 191 4. Discussion

192 Analogies are often drawn between dust devils on Mars and on Earth, primarily due  
 193 to the lack of *in situ* measurements of Martian dust devil characteristics. Terrestrial dust  
 194 devil activity has been observed to peak in the afternoon: Sinclair (1969) described dust  
 195 devil observations in Arizona spanning 1000 to 1630 and reaching a maximum between  
 196 1300 and 1400; Snow and McClelland (1990) observed dust devils in New Mexico starting

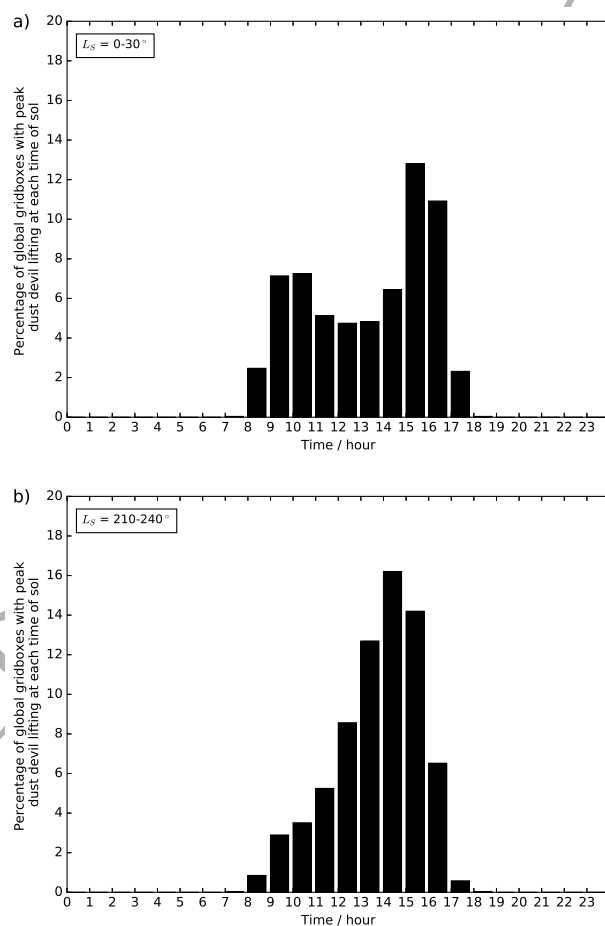


Figure 2: Histograms displaying the diurnal timing of peak dust devil lifting as a percentage of all surface gridboxes. a) Dust devil lifting averaged across  $L_S = 0-30^\circ$  (identical data displayed in Figure 1): a clear bimodal curve can be seen in the data, with a morning peak between 0900 and 1100 and an afternoon peak between 1500 and 1700. b) Dust devil lifting averaged across  $L_S = 210-240^\circ$ : the unimodal curve peaks between 1400 and 1500.

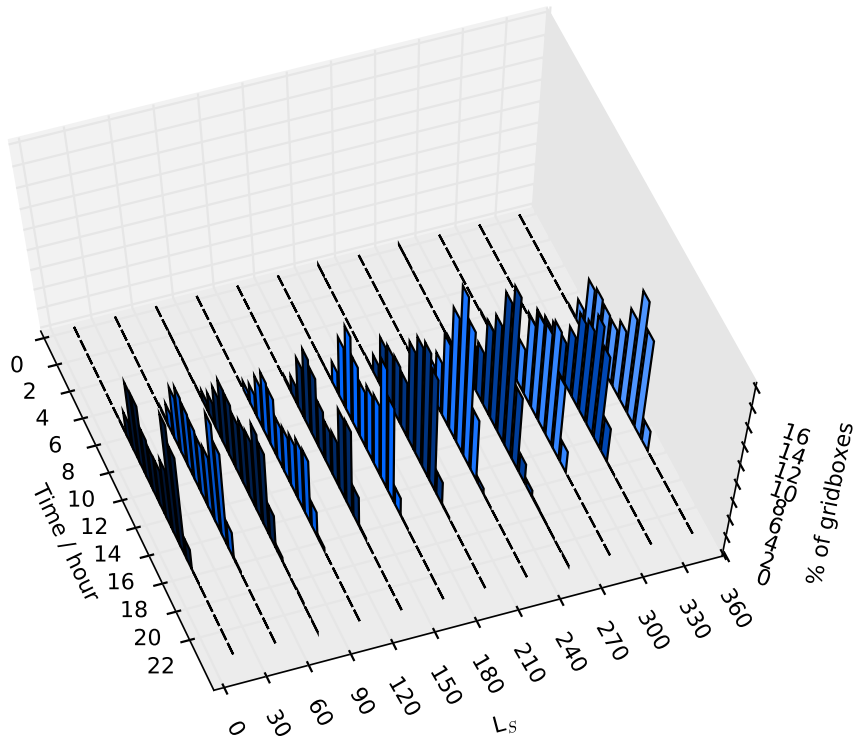


Figure 3: Histogram displaying the diurnal timing of peak dust devil lifting as a percentage of all surface gridboxes. These results show data through a full Martian year, averaged across sections covering  $30^\circ$   $L_S$ . The bimodal distribution in peak dust devil lifting timing is visible for the sections covering  $L_S = 0-210^\circ$  (Northern Hemisphere spring and summer), while the sections plotted  $L_S = 210-330^\circ$  (Northern Hemisphere autumn and winter) display a unimodal distribution. The shape of the section covering  $L_S = 330-360^\circ$  suggests a returning shift to a bimodal distribution.

197 around 1100, peaking in number between 1230 and 1300, and ending by 1600; Oke et al.  
 198 (2007) reported dust devil observations in New South Wales, Australia, occurring between  
 199 1120 and 1740, with activity peaking between 1400 and 1540; and Lorenz and Lanagan  
 200 (2014) used pressure data to identify dust devil events in Nevada starting around 0900,  
 201 peaking twice in the afternoon (shortly before 1400 and around 1600) and lasting until  
 202 2000.

203 While Figure 1 shows gridboxes across the surface of Mars displaying peaks in dust  
 204 devil lifting during both the morning and the afternoon, Figure 6 shows in more detail  
 205 that some individual gridboxes display morning-only dust devil lifting, some display  
 206 afternoon-only dust devil lifting, and others display more extended dust devil lifting  
 207 through the course of the sol, including occasional bimodal lifting.

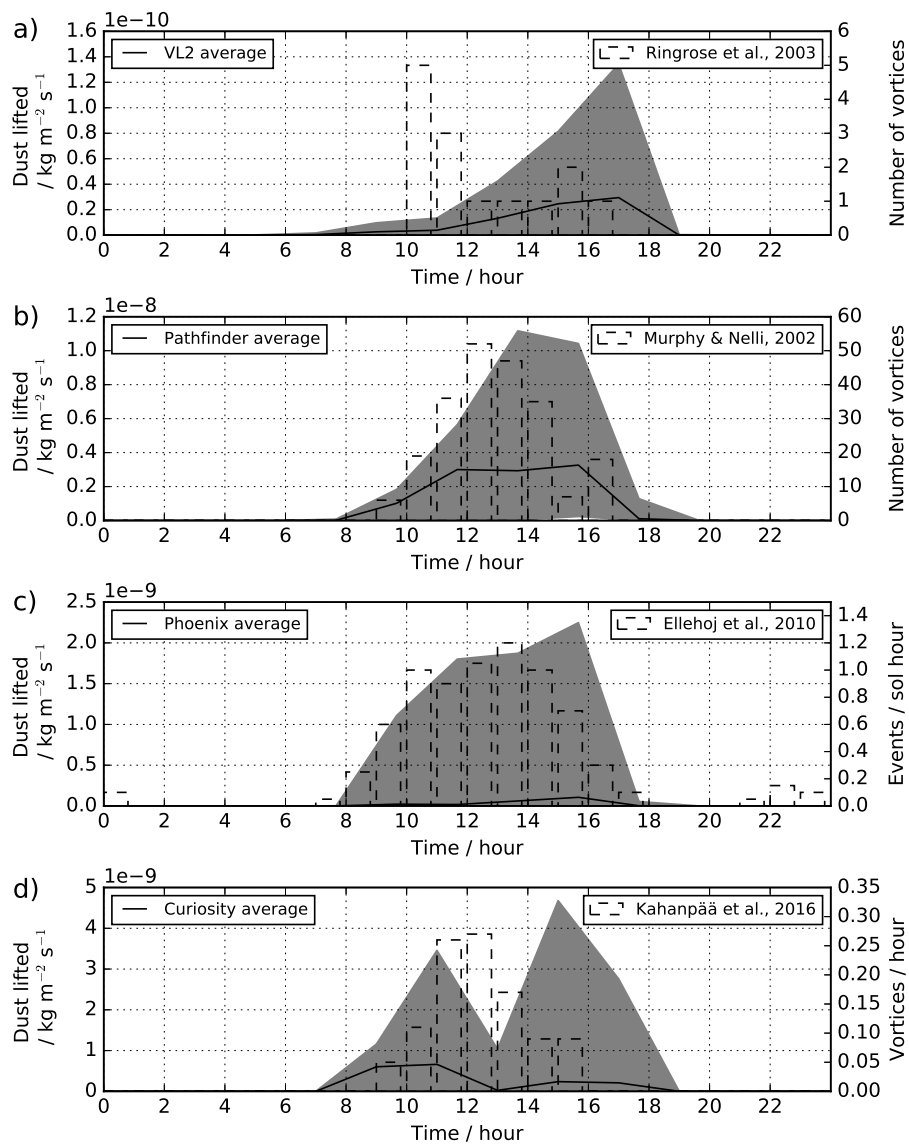


Figure 4: Hourly dust devil lifting in the vicinity of three lander sites, plotted against the left vertical axes. For each site, the average is displayed as a black solid line, and the grey shading is the envelope of all results produced during the relevant time period. Plotted against the right vertical axes are data from the comparison studies. a) VL2 landing site,  $L_S = 117\text{-}148^\circ$ , plotted against data from Ringrose et al. (2003); b) Pathfinder landing site,  $L_S = 140\text{-}190^\circ$ , plotted against data from Murphy and Nelli (2002); c) Phoenix landing site,  $L_S = 77\text{-}148^\circ$ , plotted against data from Ellehoj et al. (2010); d) MSL Curiosity site,  $L_S = 157^\circ \text{ MY31}$  to  $L_S = 157^\circ \text{ MY32}$ , plotted against data from Kahanpää et al. (2016).

#### 208 4.1. Diurnal variability within the dust devil parameterisation

209 The root of the timing variability in peak dust devil lifting can be found by examining  
 210 the component variables within Equation 1. The values of  $\alpha_D$ ,  $c_p$ , and  $C_D$  were constant

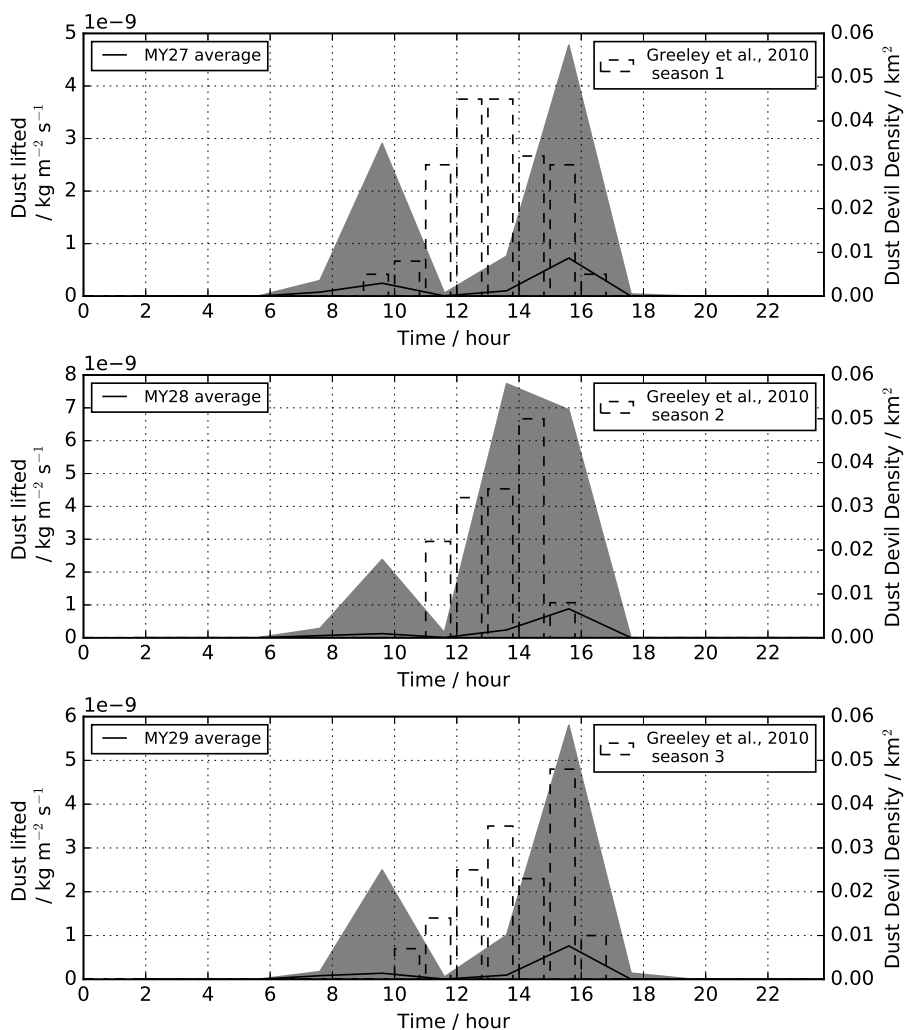


Figure 5: Hourly dust devil lifting in the vicinity of the MER Spirit site across the three Mars years considered, plotted against the left vertical axes. Each average (black solid line) is displayed, and the grey shading encompasses all results produced during the time periods (each  $L_S = 170\text{-}359^\circ$ ). Plotted against the right vertical axes are data from the comparison study by Greeley et al. (2010).

211 during this simulation, so cannot in themselves cause the diurnal variation displayed in  
 212 the dust devil lifting. We now describe the diurnal variations of the thermodynamic  
 213 efficiency  $\eta$ , the near-surface atmospheric density  $\rho$ , and the surface-to-atmosphere tem-  
 214 perature gradient,  $(t_{\text{surf}} - t_{\text{atm}})$ .

215 The diurnal variation of  $\eta$  follows the diurnal variation of the depth of the CBL. The  
 216 depth of the CBL, represented by  $p_{\text{surf}} - p_{\text{top}}$ , is driven directly by the increase of heat  
 217 in the lower portion of the atmosphere, arising from insolation-driven heating of both  
 218 the surface and the near-surface atmosphere (Spiga et al., 2010). As such, the depth of

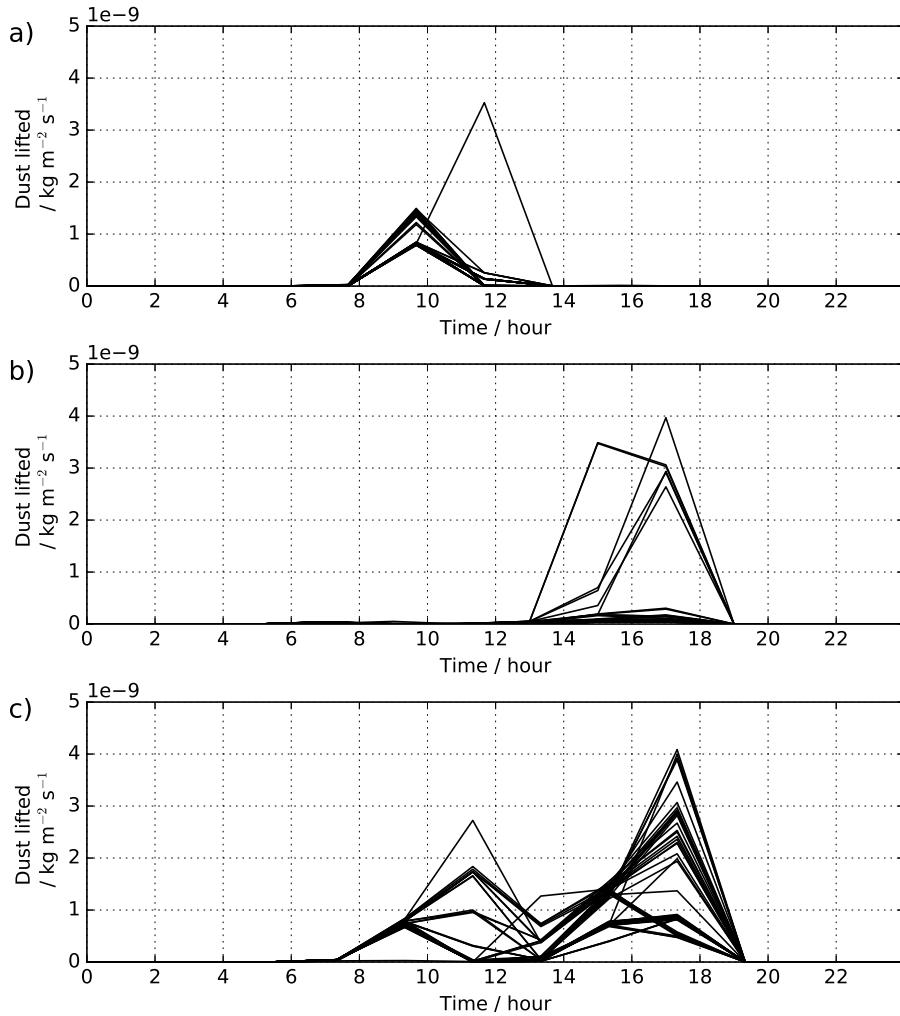


Figure 6: Dust devil lifting within individual gridboxes through  $L_S = 120-150^\circ$ ; this time of year was chosen as an example period. Each plotted line corresponds to the dust devil lifting through one sol (60 sols in total). The plots show varying diurnal timings of dust devil lifting: a) morning-only dust devil lifting (gridbox centred on  $-12.5^\circ\text{N}$ ,  $175^\circ\text{E}$ ), b) afternoon-only dust devil lifting ( $37.5^\circ\text{N}$ ,  $75^\circ\text{E}$ ), and c) through-sol dust devil lifting, displaying a nominal bimodal distribution ( $27.5^\circ\text{N}$ ,  $-10^\circ\text{E}$ ).

219 the CBL follows the diurnal pattern of heating in the lowest levels of the atmosphere:  
 220 CBL depth steadily increases during the morning, reaches a peak in the late afternoon,  
 221 and decreases (more rapidly) in the evening. While the local absolute depth of the CBL  
 222 varies greatly over the planet depending on local surface height (Hinson et al., 2008), the  
 223 diurnal pattern of the CBL depth is consistent due to its dependence on insolation. The  
 224 value of  $\eta$  will therefore peak in late afternoon, its local value determined by the local  
 225 depth of the CBL; a CBL depth of  $\sim 5$  km results in  $\eta \sim 0.06$  and a CBL depth of  $\sim 8$  km  
 226 results in  $\eta \sim 0.08$  (where  $\chi = 0.256793$ ).

227 Figure 7 shows example  $\eta$  curves calculated for an equatorial location (the gridbox  
 228 centred on  $-2.5^\circ\text{N}$ ,  $-5^\circ\text{E}$ , which is the landing site of MER Opportunity) at around  $L_S \approx$   
 229  $245^\circ$ , in a year experiencing a low atmospheric dust loading (MY24). It can be seen that  
 230 the example curve of  $\eta$  increases during the morning, reaches a maximum shortly after  
 231 peak insolation, and then decays more quickly in the evening.

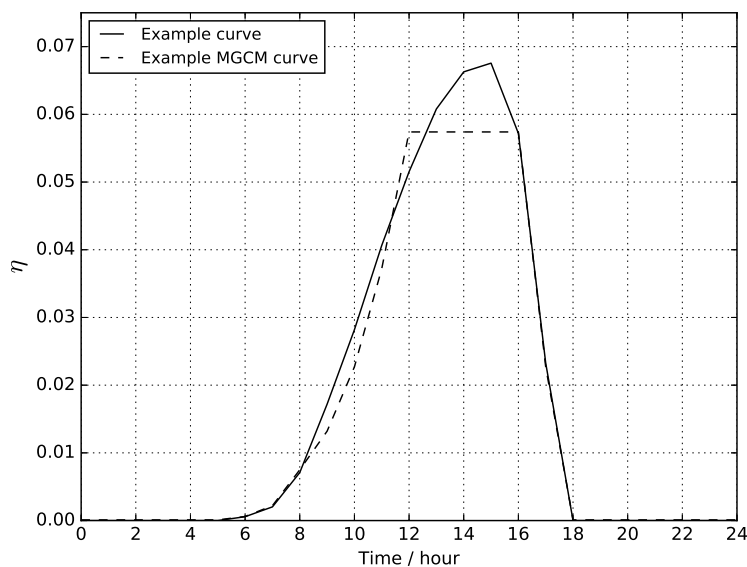


Figure 7: The example  $\eta$  curve (solid line) was calculated using a representative diurnal CBL depth curve extracted from the Mars Climate Database (Lewis et al., 1999). The example MGCM  $\eta$  curve (dashed line) illustrates how the calculation of  $\eta$  within the model can be affected by the discretisation of atmospheric layers. This truncation/quantisation effect is due to the depth of the model's atmospheric layers, which are shallow close to the surface (only tens of metres deep in the lowest layers) but increase in depth as altitude increases ( $\sim 2000$  m deep at an altitude of 5 km).

232 Near-surface atmospheric density,  $\rho$ , varies widely by location, driven by local varia-  
 233 tion in the near-surface atmospheric pressure. Atmospheric density curves from surface  
 234 locations at extremes of altitude are plotted in Figure 8. Although the absolute values  
 235 plotted are substantially different, the diurnal variation in near-surface density is similar  
 236 in both locations.

237 The temperature gradient between the surface and the near-surface atmosphere,  
 238  $(t_{\text{surf}} - t_{\text{atm}})$ , has a predictable diurnal cycle, the magnitude of which is dependent on lat-  
 239 itude and time of year. Surface temperature peaks at maximum insolation, around 1300  
 240 local time, while near-surface atmospheric temperature peaks between 1600 and 1700.  
 241 This lag between the temperature curves produces a maximum in  $(t_{\text{surf}} - t_{\text{atm}})$  that oc-  
 242 curs slightly earlier in the sol than the peak surface temperature. Although surface and  
 243 near-surface temperatures vary by a large amount with changing latitude and altitude,  
 244 the timings of the peaks in the temperature curves remain relatively consistent. Figure  
 245 9 displays the temperature curves associated with a gridbox in the region of Meridiani  
 246 Planum.

247 As  $\eta$ ,  $\rho$ , and  $(t_{\text{surf}} - t_{\text{atm}})$  follow smooth, predictable diurnal patterns, these variables

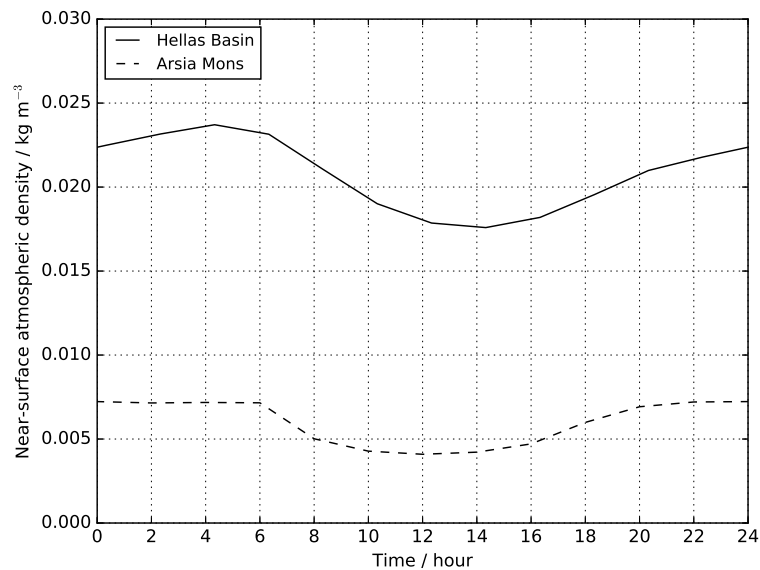


Figure 8: Near-surface atmospheric density at two locations: within Hellas basin (at an altitude  $\sim 6.7$  km below Mars datum) and in the vicinity of Arsia Mons (at an altitude  $\sim 15.5$  km above Mars datum). Values are averaged over  $L_S = 240-270^\circ$ . The shape of the diurnal curve is similar for both sites through the length of a sol.

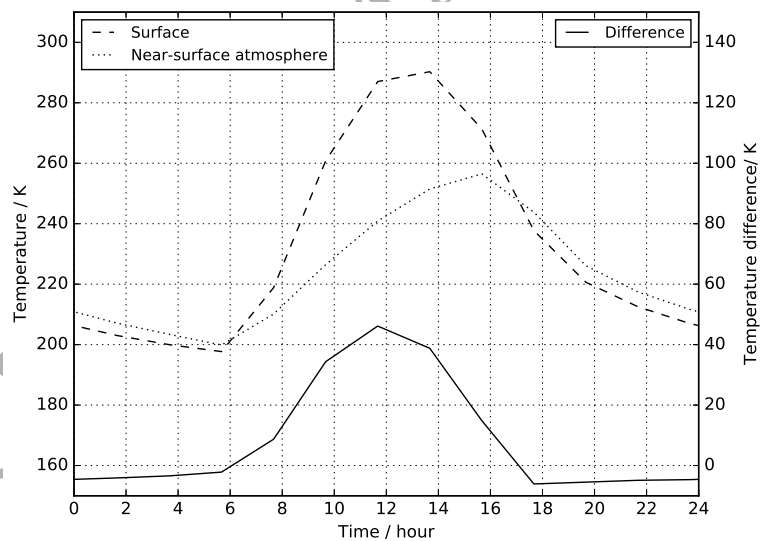


Figure 9: Surface temperature and near-surface atmospheric temperature curves plotted against the left axis; temperature difference ( $t_{\text{surf}} - t_{\text{atm}}$ ) plotted against the right axis. Values are averaged over  $L_S=240-270^\circ$ , this gridbox is centred on  $-2.5^\circ\text{N}$ ,  $-5^\circ\text{E}$ . The peak in temperature difference occurs around 1200, leading the peak in surface temperature.



248 provide no insight into the short-term variability of dust devil lifting. Both  $\eta$  and ( $t_{\text{surf}} -$   
 249  $t_{\text{atm}}$ ) must be greater than zero for any dust devil lifting to occur, but their through-sol  
 250 variation follows predictable diurnal patterns. The only component in Equation 1 that  
 251 does not follow a smooth, predictable curve through each sol is the near-surface wind  
 252 speed  $U$ . This variable is calculated from the zonal and meridional wind components  
 253 of the large scale winds within the lowest model layer of the atmosphere (typically at a  
 254 height of  $\sim 5$  m above the surface), and can be highly variable throughout the course of  
 255 one sol. Figure 10 shows an example of the variability present in near-surface wind speed.  
 256 Dust devil lifting within the same gridbox is also shown: in this particular gridbox the  
 257 timing of the dust devil lifting is broadly distributed through daylight hours. Figure 11  
 258 shows the near-surface wind speeds associated with the examples of morning-only and  
 259 afternoon-only dust devil lifting plotted in Figure 6.

260 Figure 12 shows histograms of the diurnal timing of peak near-surface wind speeds  
 261 through the course of a simulated Martian year. A seasonal shift is evident, moving be-  
 262 tween a bimodal distribution of timings (during Northern Hemisphere spring and summer)  
 263 and a unimodal distribution (during Northern Hemisphere autumn and winter).  
 264 This pattern closely matches the distributions identified in diurnal timings of peak dust  
 265 devil lifting (see Figure 3).

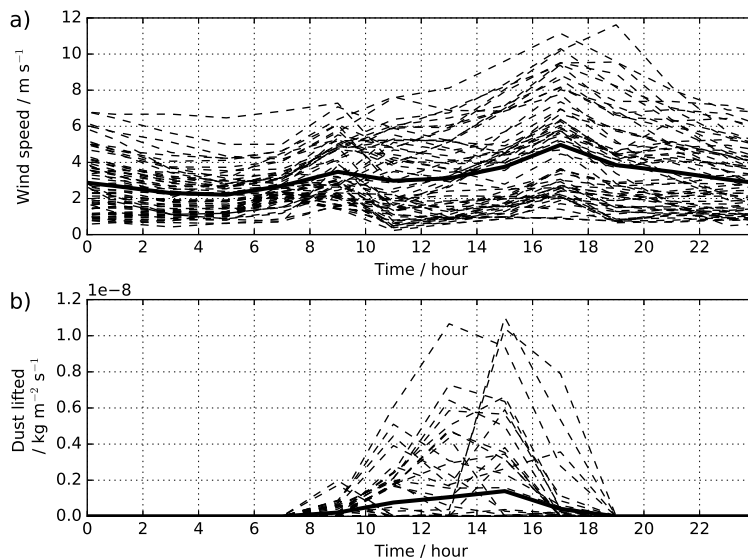


Figure 10: Near-surface wind speeds and dust devil lifting within an individual gridbox ( $47.5^{\circ}\text{N}$ ,  $135^{\circ}\text{E}$ ) through the period  $L_S = 0-30^{\circ}$ . Each dashed line corresponds to values through one sol (60 sols in total), the heavy solid line shows the average of this period. Both panels show the variability of the plotted values: a) wide variation in the amplitude of wind speeds, b) variation in the timing and amplitude of dust devil lifting.)

266 From the discussion above it can be concluded that the variability in the timing of  
 267 dust devil lifting depends primarily on the speed of the near-surface wind. Insolation  
 268 is the root driver of Martian dust devil formation: the period of the sol in which there  
 269 is a positive value of sensible heat at the planet's surface provides an envelope of time

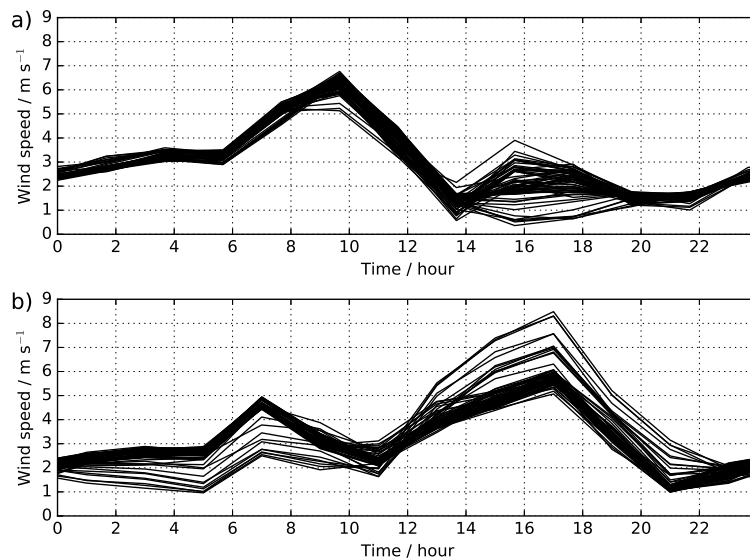


Figure 11: Near-surface wind speeds within individual gridboxes through the period  $L_S = 120-150^\circ$ . Each plotted line corresponds to the varying wind speed through one sol (60 sols in total). a) gridbox centred on  $-12.5^\circ\text{N}$ ,  $175^\circ\text{E}$ , b) gridbox centred on  $37.5^\circ\text{N}$ ,  $75^\circ\text{E}$ . Compare with panels a) and b) in Figure 6.

270 during which dust devils *can* form. Precisely *when* dust devils form within that timing  
 271 envelope is governed by the instantaneous near-surface wind speed, at least, as described  
 272 in the dust devil parameterisation schemes used in MGCMs. Figure 13 shows how the  
 273 wind speed and temperature terms of the parameterisation vary globally, and highlights  
 274 examples of the correlation between these terms and the resultant level of dust devil  
 275 lifting.

276 The magnitude and direction of the near-surface wind flow arises from a complex  
 277 interaction of local and large scale influences. Solar heating of the atmosphere drives  
 278 global diurnal thermal tides, the smaller-scale flow of which is affected by more local  
 279 variations in surface properties (Wilson and Hamilton, 1996). Variations in topography  
 280 give rise to slope winds (upslope during daylight hours and downslope during the night),  
 281 and contrasts in surface thermal properties (such as variations in albedo and thermal  
 282 inertia, or polar ice cap edges) have a changing effect on the flow of local-scale winds  
 283 throughout the diurnal heating cycle (Read and Lewis, 2004). Interactions between these  
 284 locally-forced wind flows and large-scale, regional circulations (e.g. lower-level Hadley  
 285 circulation) must also be considered (Toigo and Richardson, 2003).

286 Observations of terrestrial dust devil activity suggest that near-surface winds must be  
 287 present for the initiation of dust devils, but that high wind speeds may inhibit their for-  
 288 mation: Sinclair (1969) observed dust devil activity decreasing as wind speeds increased;  
 289 Oke et al. (2007) observed dust devils only when ambient wind speeds were between 1.5  
 290 and  $7.5 \text{ m s}^{-1}$ ; Kurgansky et al. (2010) observed an increase in dust devil numbers when  
 291 wind speeds were between 2 and  $8 \text{ m s}^{-1}$ . It has been proposed that terrestrial convective  
 292 vortices forming in high wind conditions will be rapidly destroyed by a shearing of the

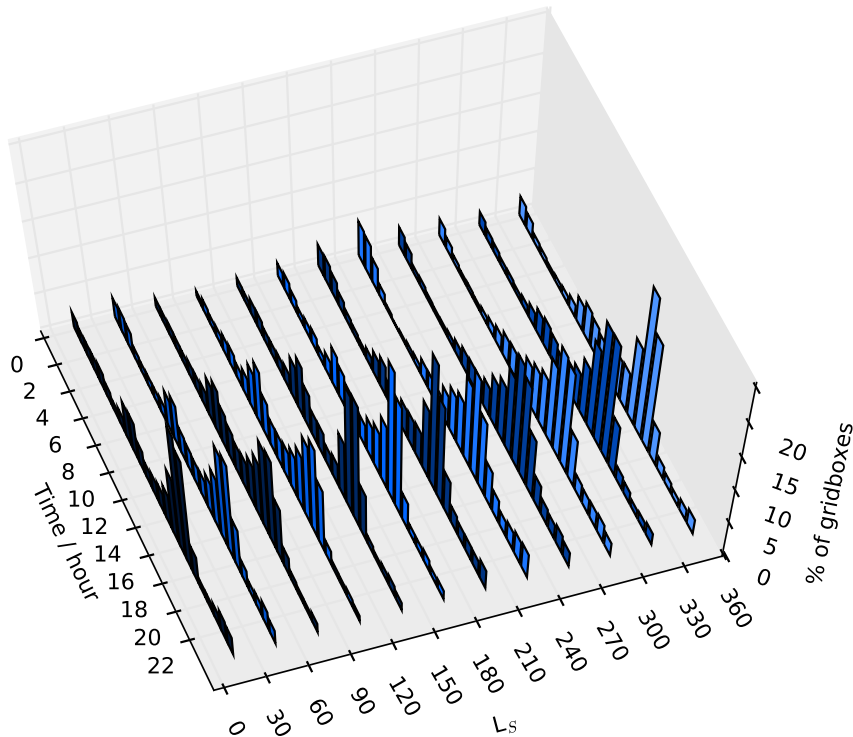


Figure 12: Histogram displaying the diurnal timing of peak near-surface wind speeds as a percentage of all surface gridboxes. A bimodal distribution in timings is evident in the sections covering  $L_S = 0-210^\circ$  while the sections plotted  $L_S = 210-300^\circ$  display a unimodal distribution. The shape of the sections through  $L_S = 300-360^\circ$  suggest a returning shift to a bimodal distribution. Compare with the similar annual variation in peak dust devil lifting timings in Figure 3.

293 upper portion of the vortex from the lower portion due to the wind speeds present (Oke  
 294 et al., 2007), and analyses of terrestrial dust devil populations have found that favourable  
 295 conditions for dust devil formation can be modelled using increasing wind speeds to curb  
 296 the level of dust devil activity (Lyons et al., 2008; Jemmett-Smith et al., 2015). Con-  
 297 versely, Toigo et al. (2003) completed high resolution numerical simulations of Martian  
 298 dust devils, in which dust devils formed in ‘no wind’ and ‘high wind’ scenarios but did  
 299 not form in low or medium wind scenarios, potentially highlighting another incidence in  
 300 which terrestrial dust devil theory cannot be directly applied to the Martian phenomena.

301 Some dust devils on Mars have been identified moving considerably faster than ter-  
 302 restrial dust devils. Martian dust devils have been observed to travel in the direction of  
 303 the ambient wind (Stanzel et al., 2008; Reiss et al., 2014), with horizontal speeds of 27  
 304  $\text{m s}^{-1}$  identified from surface observations (Greeley et al., 2010), and up to 59  $\text{m s}^{-1}$  cal-  
 305 culated from orbital images (Stanzel et al., 2008). Limited data is available on Martian  
 306 near-surface wind speeds (Balme et al., 2012), but if there is a systematic inhibition of  
 307 Martian dust devil formation due to high wind speeds, it occurs at much higher speeds

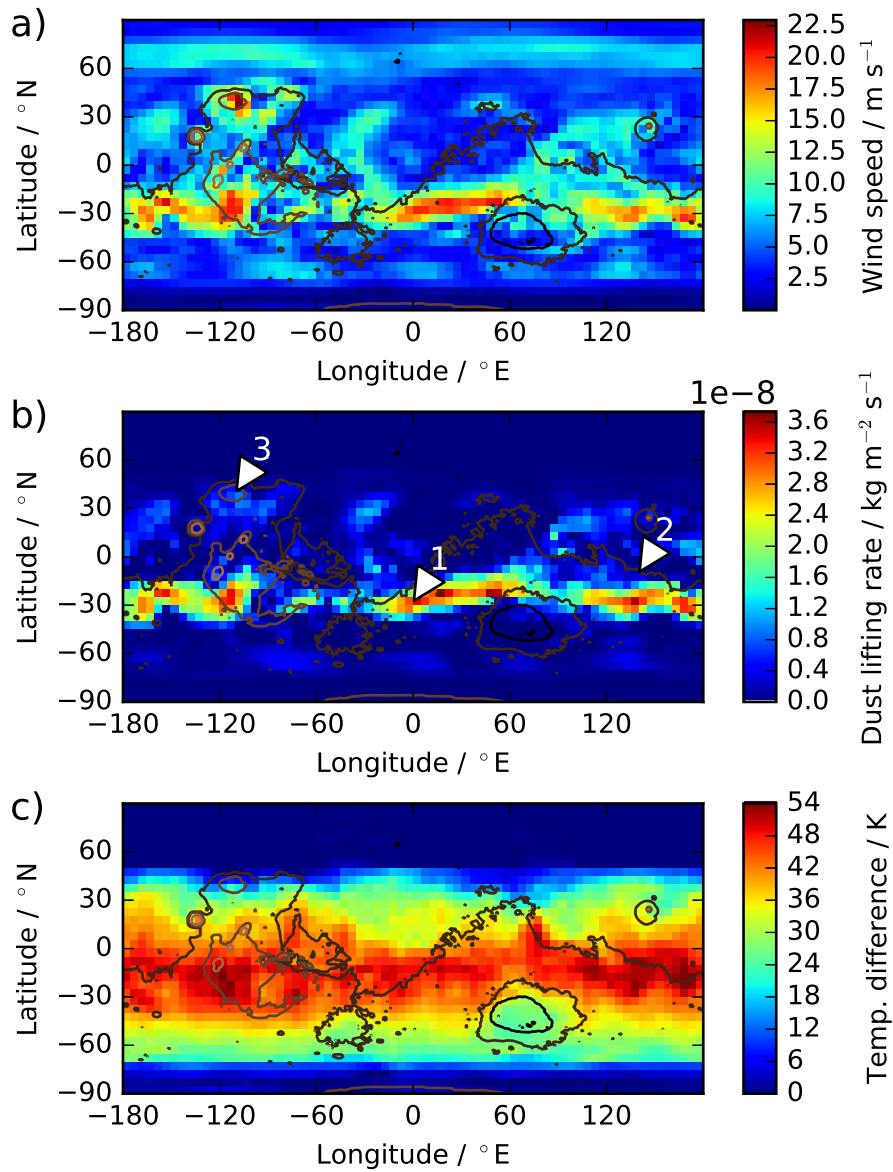


Figure 13: Global map of a) near-surface wind speeds, b) dust devil lifting and c) surface-atmosphere temperature difference, ( $t_{\text{surf}} - t_{\text{atm}}$ ). All gridboxes are displayed at a local time of 1300, providing a global picture of activity at one specific time of sol. Values are averaged over  $L_S = 240-270^\circ$ . Dust devil lifting occurs within the ‘permitted’ envelope represented by  $(t_{\text{surf}} - t_{\text{atm}}) > 0$ , but at specific locations governed by the wind speeds. Compare the locations labelled in panel b): 1.  $-28^\circ\text{N}$ ,  $0^\circ\text{E}$  (high temperature difference, high winds, high lifting), 2.  $-10^\circ\text{N}$ ,  $140^\circ\text{E}$  (high temperature difference, low winds, low lifting), 3.  $40^\circ\text{N}$ ,  $-110^\circ\text{E}$  (low temperature difference, high winds, low lifting).

308 than those proposed for terrestrial dust devils.

#### 309 4.2. Comparisons with observations

310 We can compare our global results with observations of global Martian dust devil  
311 activity, although there have been limited surveys of dust devil diurnal variation using  
312 orbital observations. It should be noted, however, that the total number of dust devils  
313 observed in orbital images is necessarily limited by the resolution of those images. Mars  
314 landers and rovers have observed many small dust devils that could not currently be seen  
315 from space (Stanzel et al., 2006).

316 Some dust devil surveys are temporally constrained by the viewing angle provided  
317 by the platform: for example, surveys using Mars Global Surveyor (MGS) Mars Orbital  
318 Camera (MOC) images are restricted to a local time of 1300-1500 (Cantor et al., 2006).  
319 Stanzel et al. (2008) used an observation set that was not so temporally restricted to  
320 survey dust devils and their characteristics: Mars Express High Resolution Stereo Camera  
321 (HRSC) images. All seasons of the year were included in their image survey, and the  
322 regions selected for scrutiny were identified as ‘active dust devil areas’ in previous studies;  
323 they found a strong peak in dust devil numbers between 1400 and 1500, with a smaller  
324 peak between 1200 and 1300. The morning peak in dust devil lifting evident in our  
325 results was not identified by this survey, in which dust devils were only observed in  
326 images captured after 1100. HRSC images span 0600 to 2000.

327 We compare our results directly with results from the comparison studies mentioned  
328 in Section 3 (and displayed in Figures 4 and 5). The comparisons are detailed below and  
329 summarised in Table 2.

330 Ringrose et al. (2003) identified 38 convective vortices in pressure data from the first  
331 60 sols of the Viking Lander 2 mission. The anticipated afternoon peak was seen, although  
332 in the early afternoon (1300-1330) rather than the mid-afternoon. A morning peak was  
333 also evident, between 1000 and 1030. The authors commented on this morning peak,  
334 proposing that it was due to convective vortices produced by the local wind interacting  
335 with the body of the lander, rather than ‘naturally generated’ dust devils. In contrast to  
336 that study, our averaged results for this location show a strong peak in dust devil lifting  
337 during the late afternoon, around 1700 (Figure 4a). Our results show limited dust devil  
338 lifting in the morning, although lifting does still occur ahead of the afternoon peak. Due  
339 to the suggestion by Ringrose et al. (2003) that at least some of the observed morning  
340 vortices were likely false positives, potentially excluding up to four of the nine morning  
341 observations, we have described the match between the observations and our results as  
342 a ‘partial match’ in Table 2.

343 Murphy and Nelli (2002) used pressure data from the full length of the Pathfinder  
344 mission ( $L_S = 142-183^\circ$ ) to identify 79 pressure signatures indicative of atmospheric  
345 vortices passing over or near the lander. Maximum vortex activity was observed between  
346 1200 and 1300. Our averaged results for this location show afternoon dust devil lifting  
347 intensity that is relatively constant between 1200 and 1600, with a slight dip in activity  
348 around 1400 (Figure 4b). However, the full envelope of our results displays a distribution  
349 similar in shape to the distribution observed by Murphy and Nelli (2002), although it is  
350 shifted later in the sol by approximately one hour.

351 Ellehoj et al. (2010) considered data from the whole length of the Phoenix mission and  
352 identified 502 “probable” convective vortices from drops in pressure data. The analysis

353 of these vortices is split by the authors into vortices identified between  $L_S = 77-111^\circ$   
 354 and vortices identified between  $L_S = 111-148^\circ$ , due to their observation that the ‘dust  
 355 devil season’ at the lander location began around  $L_S = 111^\circ$ . The vortex observations  
 356 through  $L_S = 77-111^\circ$  peak around 1200. The vortex observations through the dust devil  
 357 season of  $L_S = 111-148^\circ$  display a double peak: a morning peak around 1100 and an  
 358 afternoon peak around 1300. The authors propose that the number of vortices actually  
 359 peaks around 1200 through the latter period as well, and that this apparent bimodal  
 360 curve is due to a repeated  $\sim 30$  minute gap in observations around mid-sol: the period  
 361 at which the lander paused operations every sol in order to complete data transfer. Our  
 362 averaged results for this location show extremely low levels of dust devil lifting that peak  
 363 around 1600 (Figure 4c). This low average is due to the fact that an extended section of  
 364 our  $L_S = 77-111^\circ$  period does not contain any dust devil lifting at all. The increase  
 365 in observed devil activity identified by Ellehoj et al. (2010) as the local start of the dust  
 366 devil season does not occur in our results until  $L_S \approx 144^\circ$ . The majority of the dust  
 367 devil lifting results displayed in Figure 4c are from the period  $L_S = 144-148^\circ$ . Although  
 368 therefore covering a limited period of time, the diurnal distribution of these results is  
 369 quite similar in shape and timing to the distribution observed by Ellehoj et al. (2010),  
 370 albeit with a sharp spike around 1600 that is missing from the observed data.

371 Greeley et al. (2010) used images captured by the Spirit rover during three dust devil  
 372 seasons, each of which started at a similar time of year ( $L_S \approx 181^\circ$ ). More dust devils  
 373 were observed in the first dust devil season than in the following two seasons (respectively  
 374 502, 101 and 127 dust devils). The number of images taken during the latter two seasons  
 375 was limited due to power considerations, and observations were either truncated (by a  
 376 local dust storm in the second season) or inhibited by the rover being in less favourable  
 377 locations for viewing and imaging dust devils. With regards to the time-of-sol for peak  
 378 dust devil activity, results from this multi-year survey are mixed (Figure 5). Dust devil  
 379 season 1 shows a broad peak of ‘dust devil density’ between 1200 and 1400, season 2 has  
 380 a sharper peak between 1400 and 1500, and season 3 shows a small peak between 1300  
 381 and 1400 and a larger peak between 1500 and 1600.

382 Our results for this location are similar across the three simulated years matching  
 383 the studied periods, with all three sets of results displaying bimodal distributions of dust  
 384 devil lifting. The results envelopes for all three years show a small peak in morning lifting  
 385 (consistently between 0900 and 1000) and a larger peak in afternoon lifting. Our Year 1  
 386 results are not a good match for the study’s season 1 results: our results lack the near  
 387 mid-sol peak of the study observations, although Greeley et al. (2010) did identify dust  
 388 devils during both the morning and afternoon periods of our results envelope. Year 2  
 389 more closely matches the Greeley et al. (2010) season 2 results, with a broader afternoon  
 390 peak spanning 1300 to 1600, while observations peaked between 1400 and 1500. Our  
 391 Year 3 results again lack the mid-sol lifting evident in the season 3 observations, but the  
 392 timing of the afternoon peak shows a good match between results and observations.

393 Kahanpää et al. (2016) identified 252 likely convective vortices in MSL Curiosity  
 394 pressure data recorded during the first full year of operations, 668 sols from  $L_S = 157^\circ$   
 395 MY31 to  $L_S = 157^\circ$  MY32. Maximum vortex activity was observed between 1100 and  
 396 1300. Our results for this location show a strong bimodal distribution of lifting, with  
 397 activity peaking at 1100 and 1500 (Figure 4d). The morning peak is an hour earlier than  
 398 the observed peak in activity, but is similar in profile. The peak in afternoon activity is  
 399 not evident in the observations, although vortices were detected in the afternoon. (For

400 completeness, we also considered the vortex activity at Gale crater reported by Steakley  
 401 and Murphy (2016). Those authors identified a similar peak in vortex numbers between  
 402 1100 and 1300, reporting 245 vortices during the first 707 sols of the mission. We consider  
 403 their results a close enough match to those of Kahanpää et al. (2016) that we will use  
 404 only the latter for comparison.)

405 The comparison between our results and the various lander/rover study results does  
 406 not always give a good match, but there are several caveats to note: (i) the resolution  
 407 at which the simulation was completed results in gridboxes that cover several hundred  
 408 square kilometres in area. The data produced in such a simulation relate to quantities  
 409 present in these large-scale gridboxes, not at specific local points upon the surface. The

Lander site	MGCM results	Observation results	Comment on match
VL2	Strong afternoon peak (1700)	Strong peak 1000-1100, second peak 1500-1600	Partial match: morning lifting present but limited, afternoon lifting late
Pathfinder	Strong afternoon peak (1400)	Strong peak 1200-1300	Good match in shape of distribution, timing similar
Phoenix	Broad span, sharp peak around 1600	Broad span, peaking 1300-1400	Good match to timing of distribution
MER Spirit	Morning and afternoon peaks	Peak spanning mid-sol	Minimal match: mid-sol peak not seen
		Mid-afternoon peak 1400-1500	Good match: afternoon lifting encompasses most observations
		Mid-sol lifting, afternoon peak 1500-1600	Partial match: mid-sol peak not seen but afternoon peak matches observations
MSL Curiosity	Late morning (1100) and mid-afternoon (1500) peaks	Strong peak 1100-1200	Partial match: morning peak early, afternoon lifting greater than observed

Table 2: Summary of MGCM dust devil lifting results and dust devil observations from the comparison studies, with comment on the match of results to observations.

410 locations used in the above comparisons provide the closest possible correlation to the  
 411 lander/rover sites; (ii) the studies that use pressure data can clearly detect vortices,  
 412 but not all vortices necessarily entrain dust; (iii) the studies that rely on image data  
 413 are limited to a certain field of view (for example, rover camera pointing) and often  
 414 restricted in the times at which images were taken (e.g. 1300-1500 for MOC images);  
 415 and (iv) although our model provides a calculation for the rate of dust lifting by dust  
 416 devils, our data contain no information on either the number or the size of the dust devils  
 417 required to lift such an amount of dust. Within this work we have made the assumption  
 418 that all Martian dust devils are similar in their dust lifting efficiency; i.e. the presence  
 419 of more dust devils will result in more dust being lifted, allowing a direct comparison  
 420 between the number of vortices recorded and the amount of lifted dust.

#### 421 4.3. Alternative simulations

422 Figures 1 to 3 show results from a simulation that used a relatively low atmospheric  
 423 dust loading. In order to check whether our results were specific only to low dust cases,  
 424 an additional simulation was completed that utilised a higher atmospheric dust loading  
 425 (corresponding to the higher levels of atmospheric dust loading observed during MY25).  
 426 The results of this simulation produce similar histogram curves to those presented in  
 427 Figure 3: peak dust devil lifting occurs during both the morning and the afternoon  
 428 across the globe during the Northern Hemisphere spring and summer months, shifting  
 429 to afternoon-dominated lifting during the months approaching and retreating from peri-  
 430 helion. Figure 14 shows this shift away from morning lifting occurring slightly earlier in  
 431 the year in this simulation than in the lower atmospheric dust simulation: the ‘southern  
 432 summer’ afternoon peak in dust devil lifting begins around  $L_S = 180^\circ$ .

433 The simulations discussed so far were completed at a resolution typical of global  
 434 climate modelling:  $5^\circ$  latitude  $\times$   $5^\circ$  longitude. This results in a physical scale that  
 435 is too large to capture local variations in surface properties, particularly with regard  
 436 to small-scale topographical variability. In order to begin investigating the effect of  
 437 simulation resolution on these results, a simulation was completed at a model resolution  
 438 that corresponds to a physical resolution of  $3.75^\circ$  latitude  $\times$   $3.75^\circ$  longitude. The results  
 439 of this simulation are again similar to those presented in Figure 3.

440 It should be noted that this higher resolution simulation will still not fully capture  
 441 very local surface variations. For example, near-surface wind flows will be influenced  
 442 by topographical forcing associated with craters that are beyond the resolution of our  
 443 simulations. However, these resolutions are commonly used to investigate a number of  
 444 atmospheric processes, and our results remain pertinent to those investigations, even if  
 445 very local effects cannot be resolved.

446 The calculation of sensible heat flux,  $F_s$ , used in the dust devil parameterisation  
 447 incorporates the surface drag coefficient,  $C_D$ , which in turn depends on the surface  
 448 roughness length  $z_0$ . The value of  $z_0$  was set to the ‘standard’ value of 1 cm for the  
 449 simulations above. To check whether this simplification had any effect on the diurnal  
 450 frequency distribution of dust devil activity, a comparison simulation was performed using  
 451 a surface roughness map derived from rock abundance data (as described in Hébrard et al.  
 452 (2012)). Using a value of  $z_0$  that varies across the planet’s surface does affect the amount  
 453 of dust lifted by dust devils, but the bimodal distribution is still observed in the resulting  
 454 time-of-sol histograms.



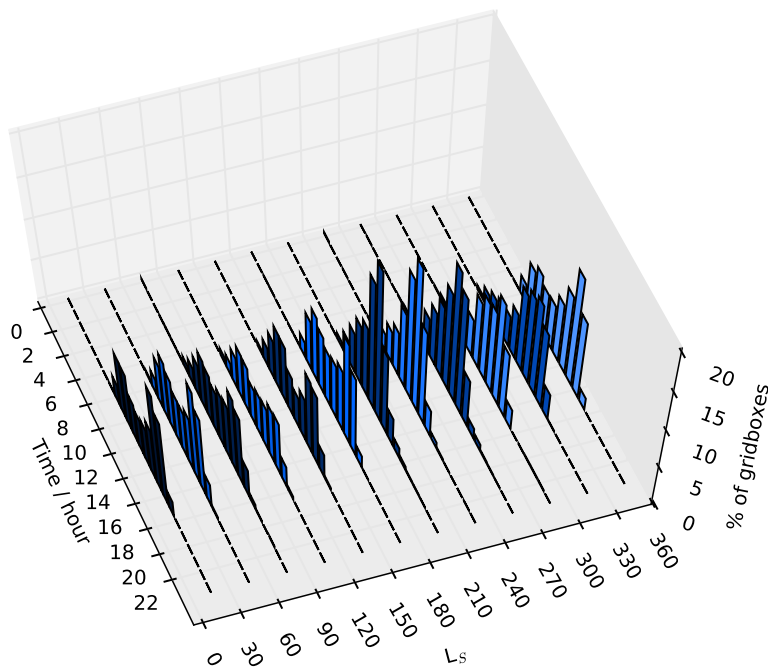


Figure 14: As Figure 3, but displaying data from a simulation using a higher atmospheric dust loading (corresponding to MY25, in which a global dust storm occurred). A bimodal distribution in peak dust devil lifting timing is visible for the sections spanning  $L_S = 0-180^\circ$  and  $L_S = 330-360^\circ$  (Northern Hemisphere spring and summer), while the sections spanning  $L_S = 180-330^\circ$  (Northern Hemisphere autumn and winter) display a unimodal distribution.

## 455 5. Summary

456 Parameterised dust devil activity depends on the sensible heat available to the dust  
 457 devil and its thermodynamic efficiency (how readily it converts available heat into work).  
 458 The thermodynamic efficiency of a dust devil is driven by the depth of the local CBL,  
 459 which follows a predictable diurnal pattern driven by atmospheric heating due to in-  
 460 solation. Most of the parameters used to calculate the sensible heat flux also follow  
 461 predictable diurnal patterns, the exception being the near-surface wind speed, which  
 462 is more stochastic in nature. It is this variability within the near-surface wind speed  
 463 that introduces variability into the diurnal timings of dust devils. The dust devil pa-  
 464 rameterisation in operation within the MGCM has been used as the basis for similar  
 465 parameterisations in the NASA Ames Mars GCM and the GFDL Mars GCM.

466 Our results show that, within MGCM simulations, more dust is lifted by dust devils  
 467 during morning hours than was previously anticipated. This disparity is primarily due to  
 468 the fact that most assumptions made about the diurnal variation of Martian dust devils  
 469 have (necessarily) been based upon observations of terrestrial dust devils. Our results  
 470 suggest two possible conclusions: that dust devil parameterisations developed for use in  
 471 MGCMs do not correctly represent diurnal dust devil behaviour, or that the generally

472 accepted description of dust devil behaviour on Mars (i.e. that dust devil activity follows  
473 a unimodal distribution that peaks around mid-sol or later) is not complete.

474 Comparing our results with those of the studies reporting surface observations, it  
475 appears that the MGCM dust devil parameterisation does reasonably represent observed  
476 dust devil diurnal behaviour in the vicinities of the lander locations. For these stud-  
477 ies, which comprise the majority of surface-based dust devil studies that discuss diurnal  
478 timings, three of the comparisons show a good match between our results and the obser-  
479 vations, three show a partial match, and one shows a minimal match (counting each of  
480 the three seasons in Greeley et al. (2010) as a separate comparison). All of these com-  
481 parison studies observed dust devils (or pressure vortices) during morning hours, and a  
482 range is seen in the timings of the data maxima across studies.

483 Studies that include diurnal surveys of dust devils using orbital observations have not  
484 identified a large number of dust devils during morning hours. These studies are few in  
485 number, probably due to the fact that many orbital observations are temporally restricted  
486 by spacecraft positioning (Fisher et al., 2005; Cantor et al., 2006), and therefore contain  
487 little information on diurnal variability. The published diurnal distribution of dust devils  
488 observed from orbit is not a good match to the majority of surface observations. As noted  
489 in Section 4.2, orbital observations are biased towards capturing large dust devils, and  
490 thus may not correctly represent the true dust devil population (Stanzel et al., 2008).

491 Our results agree with a majority of published surveys, and disagree with the as-  
492 sumption that Martian dust devil timing distributions can be simply extrapolated from  
493 terrestrial observations. Dust devil activity will not necessarily peak in the early after-  
494 noon, and local wind speeds may act as a strong governor of the timings of dust devils.  
495 We suggest that the generally accepted description of dust devil behaviour on Mars is  
496 incomplete.

497 Theories of dust devil formation may need to be further developed (or specifically  
498 tailored) in order to be truly applicable to vortices forming in a thin atmosphere over a  
499 desert that covers the entire surface of a planet. Lorenz and Radebaugh (2016) suggest  
500 that dust devils are “systematically more common” within low pressure environments.  
501 Ringrose et al. (2003) identify the possibility that Martian dust devils form earlier in  
502 the sol than terrestrial dust devils due to the lower dry adiabatic lapse rate within the  
503 Martian atmosphere; this complements the analysis of terrestrial dust devils by Jemmett-  
504 Smith et al. (2015), in which a modelled lower lapse rate resulted in a wider diurnal range  
505 of potential dust lifting activity.

506 While dust devil theories may not transfer directly between terrestrial and Martian  
507 dust devils, the parameterisation may also need improvement. One factor that must be  
508 considered is that of the input heat source driving the model dust devil ‘heat engine’.  
509 On Earth the sensible heat flux is a large factor in the total surface energy budget  
510 (Larsen et al., 2002), but on Mars the surface energy budget calculation is dominated by  
511 radiative fluxes, due to the lower density of the Martian atmosphere (Petrosyan et al.,  
512 2011). Terrestrial models of dust devils use the sensible heat flux as the dominant  
513 heat source driving their formation (e.g. Koch and Rennó (2005)); it is possible that the  
514 MGCM dust devil parameterisation should incorporate a more complex representation of  
515 the heat available for dust devil formation at the Martian surface-atmosphere boundary.  
516 A good test of the current dust devil parameterisation would be to incorporate it into a  
517 terrestrial GCM: the existing sensible heat flux formulation could be expected to produce  
518 results that are a good match for terrestrial dust devil activity (within the limited dusty

519 areas on Earth).

520 To support development of theories of Martian dust devil formation and behaviour,  
521 further surveys of dust devil observations are required. These observations should encom-  
522 pass the full diurnal period. Martian dust devil observations should also be considered  
523 within a wider meteorological context, in order to enable investigation of connections be-  
524 tween dust devils and local meteorological conditions, and allow subsequent comparison  
525 with similar studies of terrestrial dust devils (e.g. Balme et al. (2012)).

526 A near-future surface mission that may facilitate such observations is NASA's InSight  
527 (planned to carry temperature, pressure and wind sensors, and cameras (Smrekar, 2015)).  
528 Orbital images that span the diurnal period may be obtained from the Colour and Stereo  
529 Surface Imaging System (CaSSIS) instrument (Roloff et al., 2015) carried aboard ESA's  
530 ExoMars Trace Gas Orbiter.

## 531 6. Conclusions

532 In this paper we have presented the results of our investigation into the diurnal varia-  
533 tion of dust devil activity, discussed the details of the MGCM dust devil parameterisation,  
534 and compared our results with lander and spacecraft observations. In conclusion:

- 535 • The modelled dust devil activity displays a wider than anticipated diurnal range,  
536 with more activity occurring during the morning than was expected. Heating due  
537 to insolation produces conditions suitable for dust devil formation, but we identify  
538 that the diurnal variability of dust devil activity is governed by local wind speeds:  
539 higher wind speeds generate higher levels of dust devil activity.
- 540 • Our results show a good match with a number of studies reporting on surface  
541 observations of Martian dust devils, in which landers have observed a range of dust  
542 lifting diurnal distributions. We do not find a good match between our results  
543 and global surveys of Martian dust devils conducted using images obtained from  
544 orbit. However, orbital dust devil surveys are often temporally limited by spacecraft  
545 pointing restrictions.
- 546 • Theories of terrestrial dust devil formation may need to be further developed, or  
547 tailored more specifically, in order to better fit the Martian environment. More  
548 surveys of Martian dust devils are required to support this development: orbital  
549 surveys that include observations encompassing the full diurnal cycle, and surface  
550 observations that can be placed within a wider meteorological context, including  
551 local temperatures and wind speeds.

## 552 Acknowledgements

553 The authors thank the UK Space Agency for funding under grant ST/M00306X/1 and  
554 the UK Science and Technology Facilities Council for funding under grant ST/L000776/1.  
555 The authors would also like to thank two anonymous reviewers for their comments, which  
556 have helped us to improve this paper.

557 **References**

- 558 Balme, M. R., Hagermann, A., 2006. Particle lifting at the soil-air interface by atmospheric pressure  
559 excursions in dust devils. *Geophys. Res. Lett.* 33 (19), L19S01.
- 560 Balme, M. R., Metzger, S. M., Towner, M. C., Ringrose, T. J., Greeley, R., Iversen, J., 2003a. Friction  
561 wind speeds in dust devils: A field study. *Geophys. Res. Lett.* 30 (16).
- 562 Balme, M. R., Pathare, A., Metzger, S. M., Towner, M. C., Lewis, S. R., Spiga, A., Fenton, L. K., Rencó,  
563 N. O., Elliott, H. M., Saca, F. A., Michaels, T. I., Russell, P., Verdasca, J., 2012. Field measurements  
564 of horizontal forward motion velocities of terrestrial dust devils: Towards a proxy for ambient winds  
565 on Mars and Earth. *Icarus* 221 (2), 632–645.
- 566 Balme, M. R., Whelley, P. L., Greeley, R., 2003b. Mars: Dust devil track survey in Argyre Planitia and  
567 Hellas Basin. *J. Geophys. Res. Planets* 108 (E8), 5086.
- 568 Basu, S., Richardson, M. I., Wilson, R. J., 2004. Simulation of the Martian dust cycle with the GFDL  
569 Mars GCM. *J. Geophys. Res.* 109 (E11), E11006.
- 570 Basu, S., Wilson, J., Richardson, M. I., Ingersoll, A., 2006. Simulation of spontaneous and variable  
571 global dust storms with the GFDL Mars GCM. *J. Geophys. Res.* 111 (9), E09004.
- 572 Cantor, B. A., Kanak, K. M., Edgett, K. S., 2006. Mars Orbiter Camera observations of Martian dust  
573 devils and their tracks (September 1997 to January 2006) and evaluation of theoretical vortex models.  
574 *J. Geophys. Res.* 111 (E12), E12002.
- 575 Clancy, R. T., Sandor, B. J., Wolff, M. J., Christensen, P. R., Smith, M. D., Pearl, J. C., Conrath,  
576 B. J., Wilson, R. J., 2000. An intercomparison of ground-based millimeter, MGS TES, and Viking  
577 atmospheric temperature measurements: Seasonal and interannual variability of temperatures and  
578 dust loading in the global Mars atmosphere. *J. Geophys. Res.* 105 (E4), 9553.
- 579 Colburn, D. S., Pollack, J. B., Haberle, R. M., 1989. Diurnal variations in optical depth at Mars. *Icarus*  
580 79 (1), 159–189.
- 581 Ellehoj, M. D., Gunnlaugsson, H. P., Taylor, P. A., Kahanpää, H., Bean, K. M., Cantor, B. A., Gheynani,  
582 B. T., Drube, L., Fisher, D., Harri, A.-M., Holstén-Rathlou, C., Lemmon, M. T., Madsen, M. B.,  
583 Malin, M. C., Polkko, J., Smith, P. H., Tamppari, L. K., Weng, W., Whiteway, J. A., 2010. Convective  
584 vortices and dust devils at the Phoenix Mars mission landing site. *J. Geophys. Res.* 115, E00E16.
- 585 Esau, I. N., 2004. Parameterization of a surface drag coefficient in conventionally neutral planetary  
586 boundary layer. *Ann. Geophys.* 22, 3353–3362.
- 587 Ferri, F., Smith, P. H., Lemmon, M. T., Rencó, N. O., 2003. Dust devils as observed by Mars Pathfinder.  
588 *J. Geophys. Res.* 108 (E12), 5133.
- 589 Fisher, J. A., Richardson, M. I., Newman, C. E., Szwast, M. A., Graf, C., Basu, S., Ewald, S. P., Toigo,  
590 A. D., Wilson, R. J., 2005. A survey of Martian dust devil activity using Mars Global Surveyor Mars  
591 Orbiter Camera images. *J. Geophys. Res.* 110 (E3), E03004.
- 592 Forget, F., Hourdin, F., Fournier, R., Hourdin, C., Talagrand, O., Collins, M., Lewis, S. R., Read, P. L.,  
593 Huot, J. P., 1999. Improved general circulation models of the Martian atmosphere from the surface  
594 to above 80 km. *J. Geophys. Res.* 104 (E10), 24155–24175.
- 595 Greeley, R., Balme, M. R., Iversen, J., Metzger, S. M., Mickelson, R., Phoreman, J., White, B., 2003.  
596 Martian dust devils: Laboratory simulations of particle threshold. *J. Geophys. Res.* 108 (E5), 5041.
- 597 Greeley, R., Waller, D. A., Cabrol, N. A., Landis, G. A., Lemmon, M. T., Neakrase, L. D. V., Pendleton  
598 Hoffer, M., Thompson, S. D., Whelley, P. L., 2010. Gusev Crater, Mars: Observations of three dust  
599 devil seasons. *J. Geophys. Res.* 115, E00F02.
- 600 Greeley, R., Whelley, P. L., Arvidson, R. E., Cabrol, N. A., Foley, D. J., Franklin, B. J., Geissler, P. G.,  
601 Golombek, M. P., Kuzmin, R. O., Landis, G. A., Lemmon, M. T., Neakrase, L. D. V., Squyres,  
602 S. W., Thompson, S. D., 2006. Active dust devils in Gusev crater, Mars: Observations from the Mars  
603 Exploration Rover Spirit. *J. Geophys. Res.* 111 (E12), E12S09.
- 604 Hébrard, E., Listowski, C., Coll, P., Marticorena, B., Bergametti, G., Määttänen, A., Montmessin,  
605 F., Forget, F., 2012. An aerodynamic roughness length map derived from extended Martian rock  
606 abundance data. *J. Geophys. Res. Planets* 117 (E04008).
- 607 Hinson, D. P., Pätzold, M., Tellmann, S., Häusler, B., Tyler, G. L., 2008. The depth of the convective  
608 boundary layer on Mars. *Icarus* 198 (1), 57–66.
- 609 Jemmett-Smith, B. C., Marsham, J. H., Knippertz, P., Gilkeson, C. A., 2015. Quantifying global dust  
610 devil occurrence from meteorological analyses. *Geophys. Res. Lett.* 42 (4), 1275–1282.
- 611 Kahanpää, H., Newman, C. E., Moores, J., Zorzano, M.-P., Martín-Torres, J., Navarro, S., Lepinette,  
612 A., Cantor, B. A., Lemmon, M. T., Valentín-Serrano, P., Ullán, A., Schmidt, W., 2016. Convective  
613 vortices and dust devils at the MSL landing site: Annual variability. *J. Geophys. Res. Planets*.
- 614 Kahre, M. A., Hollingsworth, J. L., Haberle, R. M., Murphy, J. R., 2008. Investigations of the variability

- 615 of dust particle sizes in the martian atmosphere using the NASA Ames General Circulation Model.  
616 *Icarus* 195 (2), 576–597.
- 617 Kahre, M. A., Murphy, J. R., Haberle, R. M., 2006. Modeling the Martian dust cycle and surface dust  
618 reservoirs with the NASA Ames general circulation model. *J. Geophys. Res.* 111 (E6), E06008.
- 619 Koch, J., Rennó, N. O., 2005. The role of convective plumes and vortices on the global aerosol budget.  
620 *Geophys. Res. Lett.* 32 (18).
- 621 Kurgansky, M. V., Montecinos, A., Villagran, V., Metzger, S. M., 2010. Micrometeorological conditions  
622 for dust-devil occurrence in the Atacama Desert. *Boundary-Layer Meteorol.* 138 (2), 285–298.
- 623 Larsen, S. E., Jørgensen, H. E., Landberg, L., Tillman, J. E., 2002. Aspects of the atmospheric surface  
624 layers on Mars and Earth. *Boundary-Layer Meteorol.* 105, 451–470.
- 625 Lewis, S. R., Collins, M., Read, P. L., Forget, F., Hourdin, F., Fournier, R., Hourdin, C., Talagrand, O.,  
626 Huot, J. P., 1999. A climate database for Mars. *J. Geophys. Res.* 104 (E10), 24177.
- 627 Lorenz, R. D., Lanagan, P. D., 2014. A barometric survey of dust-devil vortices on a desert playa.  
628 *Boundary-Layer Meteorol.* 153 (3), 555–568.
- 629 Lorenz, R. D., Radebaugh, J., 2016. Dust devils in thin air: Vortex observations at a high elevation  
630 Mars analog site in the Argentinian Puna. *Geophys. Res. Lett.*
- 631 Lyons, T. J., Nair, U. S., Foster, I. J., 2008. Clearing enhances dust devil formation. *J. Arid Environ.*  
632 72 (10), 1918–1928.
- 633 Martin, T. Z., 1986. Thermal infrared opacity of the Mars atmosphere. *Icarus* 66 (1), 2–21.
- 634 Montabone, L., Forget, F., Millour, E., Wilson, R. J., Lewis, S. R., Cantor, B. A., Kass, D., Kleinböhl,  
635 A., Lemmon, M. T., Smith, M. D., Wolff, M. J., 2015. Eight-year climatology of dust optical depth  
636 on Mars. *Icarus* 251, 65–95.
- 637 Mulholland, D. P., 2012. Martian dust lifting, transport and associated processes. Ph.D. thesis, St.  
638 Anne's College, University of Oxford.
- 639 Mulholland, D. P., Read, P. L., Lewis, S. R., 2013. Simulating the interannual variability of major dust  
640 storms on Mars using variable lifting thresholds. *Icarus* 223 (1), 344–358.
- 641 Murphy, J. R., Nelli, S., 2002. Mars Pathfinder convective vortices: Frequency of occurrence. *Geophys.*  
642 *Res. Lett.* 29 (23), 2103.
- 643 Newman, C. E., Lewis, S. R., Read, P. L., Forget, F., 2002. Modeling the Martian dust cycle 1. Repre-  
644 sentations of dust transport processes. *J. Geophys. Res.* 107 (E12), 5123.
- 645 Oke, A. M. C., Tapper, N. J., Dunkerley, D., 2007. Willy-willies in the Australian landscape: The role of  
646 key meteorological variables and surface conditions in defining frequency and spatial characteristics.  
647 *J. Arid Environ.* 71 (2), 201–215.
- 648 Petrosyan, A., Galperin, B., Larsen, S. E., Lewis, S. R., Määttänen, A., Read, P. L., Rennó, N. O.,  
649 Rogberg, L. P. H. T., Savijärvi, H., Siili, T., Spiga, A., Toigo, A. D., Vázquez, L., 2011. The Martian  
650 atmospheric boundary layer. *Rev. Geophys.* 49 (3), RG3005.
- 651 Pollack, J. B., Colburn, D. S., Kahn, R., Hunter, J., Van Camp, W., Carlston, C. E., Wolf, M. R., 1977.  
652 Properties of aerosols in the Martian atmosphere, as inferred from Viking Lander imaging data. *J.*  
653 *Geophys. Res.* 82 (28), 4479–4496.
- 654 Read, P. L., Lewis, S. R., 2004. *The Martian Climate Revisited*. Springer, Praxis Publishing.
- 655 Reiss, D., Spiga, A., Erkeling, G., 2014. The horizontal motion of dust devils on Mars derived from  
656 CRISM and CTX/HIRISE observations. *Icarus* 227, 8–20.
- 657 Rennó, N. O., Burkett, M. L., Larkin, M. P., 1998. A simple thermodynamical theory for dust devils. *J.*  
658 *Atmos. Sci.* 55 (21), 3244–3252.
- 659 Ringrose, T. J., Towner, M. C., Zarnecki, J. C., 2003. Convective vortices on Mars: a reanalysis of Viking  
660 Lander 2 meteorological data, sols 1–60. *Icarus* 163 (1), 78–87.
- 661 Roloff, V., Gambicorti, L., Pommerol, A., Thomas, N., 2015. Scientific calibration and analysis of  
662 calibration data for the CaSSIS instrument of the ExoMars Trace Gas Orbiter. In: *Eur. Planet. Sci.*  
663 *Congr.* 2015.
- 664 Sinclair, P. C., 1964. Some preliminary dust devil measurements. *Mon. Weather Rev.* 92 (8), 363–367.
- 665 Sinclair, P. C., 1969. General characteristics of dust devils. *J. Appl. Meteorol.* 8 (1), 32–45.
- 666 Smith, M. D., Pearl, J. C., Conrath, B. J., Christensen, P. R., 2001. Thermal Emission Spectrometer  
667 results: Mars atmospheric thermal structure and aerosol distribution. *J. Geophys. Res.* 106 (E10),  
668 23929.
- 669 Smith, P. H., Lemmon, M. T., 1999. Opacity of the Martian atmosphere measured by the Imager for  
670 Mars Pathfinder. *J. Geophys. Res.* 104 (E4), 8975.
- 671 Smrekar, S., 2015. The InSight mission's Martian atmospheric science goals, capabilities and instrumen-  
672 tation. In: 2015 AGU Fall Meet. AGU.
- 673 Snow, J. T., McClelland, T. M., 1990. Dust devils at White Sands Missile Range, New Mexico: 1.

- 674 Temporal and spatial distributions. *J. Geophys. Res.* 95 (D9), 13707.
- 675 Spiga, A., Forget, F., Lewis, S. R., Hinson, D. P., 2010. Structure and dynamics of the convective  
676 boundary layer on Mars as inferred from large-eddy simulations and remote-sensing measurements.  
677 *Q. J. R. Meteorol. Soc.* 136, 414–428.
- 678 Stanzel, C., Pätzold, M., Greeley, R., Hauber, E., Neukum, G., 2006. Dust devils on Mars observed by  
679 the High Resolution Stereo Camera. *Geophys. Res. Lett.* 33 (11), L11202.
- 680 Stanzel, C., Pätzold, M., Williams, D., Whelley, P. L., Greeley, R., Neukum, G., 2008. Dust devil speeds,  
681 directions of motion and general characteristics observed by the Mars Express High Resolution Stereo  
682 Camera. *Icarus* 197 (1), 39–51.
- 683 Steakley, K., Murphy, J. R., 2016. A year of convective vortex activity at Gale Crater. *Icarus*.
- 684 Strausberg, M. J., Wang, H., Richardson, M. I., Ewald, S. P., Toigo, A. D., 2005. Observations of the  
685 initiation and evolution of the 2001 Mars global dust storm. *J. Geophys. Res.* 110 (E2), E02006.
- 686 Thomas, P., Gierasch, P. J., 1985. Dust devils on Mars. *Science* (80- ). 230 (4722), 175–7.
- 687 Toigo, A. D., Richardson, M. I., 2003. Meteorology of proposed Mars Exploration Rover landing sites.  
688 *J. Geophys. Res.* 108 (E12), 8092.
- 689 Toigo, A. D., Richardson, M. I., Ewald, S. P., Gierasch, P. J., 2003. Numerical simulation of Martian  
690 dust devils. *J. Geophys. Res.* 108 (E6), 5047.
- 691 Wilson, R. J., 2011. Dust cycle modeling with the GFDL Mars General Circulation Model. In: Fourth  
692 Int. Work. Mars Atmos. Model. Obs.
- 693 Wilson, R. J., Hamilton, K., 1996. Comprehensive Model Simulation of Thermal Tides in the Martian  
694 Atmosphere. *J. Atmos. Sci.* 53 (9), 1290–1325.
- 695 Zurek, R. W., 1978. Solar heating of the Martian dusty atmosphere. *Icarus* 35 (2), 196–208.